J Comput Electron (2016) 15:1521–1530
DOI 10.1007/s10825-016-0906-2

Theoretical investigation of the electronic structure and optical properties of zinc-doped magnesium oxide

Jia Wang[1] · **Yan Tu**[1] · **Lanlan Yang**[1] · **Harm Tolner**[2]

Published online: 8 October 2016

Abstract In this work, the electronic structure and optical properties of $Mg_{1-x}Zn_xO$ ($0 \leq x \leq 0.5$) are investigated within the framework of the density functional theory (DFT), the *GW* method, and the Bethe–Salpeter equation (BSE). We find that zinc doping can lower the band gap of pure MgO via the Zn 4*s* states near the Fermi level and reduce the lattice symmetry, both of which will affect the optical properties. The energy of the first absorption peak decreases as the concentration of zinc increases, so are the exciton energy and binding energy of the lowest excited state. The results nicely fit to published experimental results and are compared to those of the simple hydrogen-like atom model for excitons. As the lowest excited state is closely related to light emission at that energy according to Kasha's rule, zinc doping will lower the light emission energy of pure MgO, while still exhibiting an exciton binding energy much higher than that of k_BT at room temperature. This means that $Mg_{1-x}Zn_xO$ materials are perfectly suited for optoelectronic devices operating in the deep blue and near-ultraviolet (UV) range.

Keywords MgO · Zinc doping · Electronic structure · Deep-UV · Exciton binding energy · Optical properties

Electronic supplementary material The online version of this article (doi:10.1007/s10825-016-0906-2) contains supplementary material, which is available to authorized users.

✉ Yan Tu
tuyan@seu.edu.cn

[1] School of Electronic Science and Engineering, Southeast University, Nanjing 210096, Jiangsu, People's Republic of China

[2] Tolner Technology, De Genestetlaan 11, 5615EG Eindhoven, The Netherlands

1 Introduction

Magnesium oxide (MgO), a wide-bandgap insulator, has promising applications in electronics due its intriguing properties like low cost, non-toxicity, high-temperature resistance, optical transmittance, and rich abundance on earth. However, its applications are hindered by its large band gap of 7.8 eV, which falls into the deep ultraviolet (UV) region [1]. On the other hand, zinc oxide (ZnO) has a moderate band gap of 3.4 eV corresponding to deep blue and UV region [2]. Thus, doping zinc into MgO may lower the band gap and improve the optical properties at lower excitation energies. Moreover, the relatively large exciton binding energies of MgO (80–85 meV) [3] and ZnO (65 meV) [4] indicate that the ternary compounds $Mg_{1-x}Zn_xO$ may be promising excitonic light emitters. $Mg_{1-x}Zn_xO$ has already found its applications in electronic devices such as solar-blind (200–280 nm) UV photo detectors, UV laser diodes, and solar cells [5–7].

To date, there are numerous theoretical and experimental investigations on $Mg_{1-x}Zn_xO$ ternary compound. It shows that the band gap of $Mg_{1-x}Zn_xO$ can be tuned within the range from 3.3 to 7.8 eV [8]. By depositing MgZnO thin film on a MgO substrate, Han et al. [5] successfully fabricated a Schottky-type MSM photo detector with low dark current, in which the sub-bandgap light response is efficiently suppressed. Yoo et al. [9] have investigated the MgZnO/ZnO coaxial nanowire heterostructure and found that the formation of MgO shells on the surfaces of ZnO nanowires enhances the photoluminescence (PL) intensity. Hu [10] and Amrani [11] have calculated the electronic structure and optical properties of wurtzite $Mg_{1-x}Zn_xO$ with Mg concentration ranging from 0 to 0.5 using the DFT+U method, finding that the optical response decreases with the increasing Mg content. In spite of these theoretical and experimental

investigations, the electronic structural and optical properties of rock-salt $Mg_{1-x}Zn_xO$, which is more stable when x is less than 0.5, remain yet rather unexplored.

In this work, we investigate the electronic structures and optical properties of rock-salt $Mg_{1-x}Zn_xO$ (x = 0, 0.125, 0.25, 0375, and 0.5) theoretically. Due to the shortcomings of DFT, which severely underestimates the band gap, we use the many-particle perturbation theory-based *GW* method to correct the DFT band structure. Also, the electron–hole interaction is taken into account through the Bethe–Salpeter equation (BSE) to calculate the optical absorption spectra and the exciton binding energies. We compare these results with the hydrogen model for an exciton, by calculating the electron and hole masses directly from the curvature of the dispersion relation. This paper is organized as follows: in Sect. 2 we give the details on the models employed in our calculation; in Sect. 3, we mainly discuss the electronic structure and optical properties of $Mg_{1-x}Zn_xO$ with emphasis on the influence of zinc doping; finally in Sect. 4, we draw the conclusions.

2 Model and methodology

Figure 1a depicts the crystalline structure of pristine MgO, which is modeled as a 2 × 2 × 2 supercell. This supercell is built from the primitive cell of MgO and contains 8 magnesium atoms. The $Mg_{1-x}Zn_xO$ (x = 0, 0.125, 0.25, 0.375, and 0.5) structures are obtained by substituting 1, 2, 3, and 4 magnesium atoms in the crystalline structure of pristine MgO with zinc atoms, respectively. The most energetically favorable sites for the substitution are determined through density functional theory [12,13] (DFT) calculations, and are shown in Fig. 1a labeled as A, B, C, and D. All $Mg_{1-x}Zn_x$Ocrystals have face-centered cubic structures. The corresponding first Brillouin zone is depicted in Fig. 1b.

The electronic structurral and optical properties of $Mg_{1-x}Zn_xO$ (x = 0, 0.125, 0.25, 0.375 and 0.5) are investigated via a three-step procedure [14,15]. First, wave functions, energies, and exchange-correlation operator matrix elements are extracted from the DFT calculations. The wave functions are expanded in a plane-wave basis set with the kinetic energy cutoff of 75 Rydberg. The Brillouin zone is sampled with a 6 × 6 × 6 Monkhorst–Pack [16] k-grid. Norm-conserving Troullier–Martins [17] pseudo-potentials are employed to treat the electron–nucleus interaction. The valence electron configuration is $3s^2$ for the Mg atom, while it is $3d^{10}4s^2$ for the Zn atom. The exchange-correlation functional is the Perdew–Burke–Ernzerhof (PBE) [18] functional. All of the atomic coordinates are fully relaxed until the total energy is converged within 0.001 eV, and the forces acting on each atom are less than 0.01 eV/Å.

Then in the second step, the quasi-particle energies are evaluated via the Dyson equation [14]

$$E_{nk}^{\mathrm{QP}} = E_{nk}^{\mathrm{KS}} + Z_{nk}\left\langle \psi_{nk}\left|\sum\left(E_{nk}^{\mathrm{KS}}\right) - V_{xc}^{\mathrm{LDA}}\right|\psi_{nk}\right\rangle \qquad (1)$$

where E_{nk}^{QP} is the quasi-particle energy, E_{nk}^{KS}, ψ_{nk}, and V_{xc}^{LDA} are the energy, wave function, and exchange-correlation operator matrix elements obtained from DFT calculations in step one aforementioned, Z_{nk} is the re-normalization factor, and $\sum\left(E_{nk}^{KS}\right)$ is the frequency-dependent self-energy operator. The *GW* approximation proposed by Hedin [19,20] is applied for the self-energy operator, i.e., $\Sigma = iGW$, where G is Green's function, and W is the screened Coulomb interaction. Both G and W are built from DFT energies and wave functions, and are not iterated during the calculation. Moreover, the plasmon-pole model [21,22] proposed by Godby and Needs is employed to treat the frequency-dependency of the self-energy operator.

Finally, the excitation energies and exciton wave functions are calculated via the Bethe–Salpeter equation [15,23,24] (BSE):

$$\left(E_{ck}^{\mathrm{QP}} - E_{vk}^{\mathrm{QP}}\right)A_{vck}^{\mathrm{S}} + \sum_{v'c'k'}\left\langle v'c'k'|K^{eh}|vck\right\rangle A_{v'c'k}^{\mathrm{S}} = \Omega^{\mathrm{S}}A_{vck}^{\mathrm{S}} \qquad (2)$$

where E_{ck}^{QP} and E_{vk}^{QP} are the quasiparticle energies obtained in step two for the conduction and valence bands, respectively;

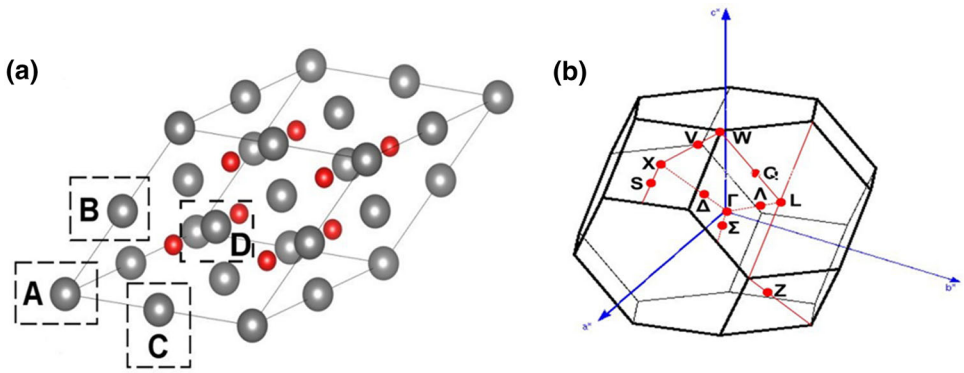

Fig. 1 **a** Crystalline structure of pure MgO. *Gray* and *red* spheres denote magnesium and oxygen atoms, respectively. The sites labeled as '*A*', '*B*', '*C*', and '*D*' are the most energetically favorable positions for substituting the first, the second, and the third magnesium atoms with zinc atoms, respectively. **b** First Brillouin zone of face-centered cubic (FCC) lattice. The *red dots* denote the high-symmetric k-points

A^S_{vck} is the coefficient of excitonic wave function on the basis of the direct product of conduction and valence wave functions; K^{eh} is the electron–hole interaction kernel; and Ω^S is the excitation energy. The imaginary part of the dielectric function, which determines the absorption spectrum, is evaluated as [25]

$$E_M(\omega) = 1 - \lim_{q\to 0} \frac{8\pi}{|q|^2 \Omega N_q} \sum_{nn'k} \sum_{mm'k} \sum_{\lambda} \rho^*_{nn'k}(q, G)\rho^*_{m'mk'} (q, G') \frac{A^{\lambda}_{n'nk}(A^*_{m'mk'})^*}{\omega - E_{\lambda}} \quad (3)$$

where q and k are the k-points in the first Brillouin zone; N_q is the number of q-points; Ω is the volume of the primitive cell; $\rho_{n'nk}(q, G)$ and $\rho_{m'mk'}(q, G')$ are convolutions of DFT wave functions in the reciprocal space; $A^{\lambda}_{n'nk}$ and $A^{\lambda}_{m'mk'}$ are , respectively, the coefficients of the excitonic wave functions; and E_{λ} is the excitation energy. To solve the BSE and calculate the dielectric function, four valence and five conduction bands are used to ensure the convergence of the absorption spectrum. The DFT and *GW*/BSE calculations are performed using the Quantum-ESPRESSO [26] and Yambo [25] codes, respectively.

3 Results and discussion

3.1 Electronic structure

As revealed by previous work, the rock-salt structure of $Mg_{1-x}Zn_xO$ is energetically more favorable than the wurtzite structure when the concentration of Zn is below 0.5. Here we consider the doping concentrations of 0 (pure MgO), 0.125, 0.25, 0.375, and 0.5 [27,28]. The equilibrium lattice constants determined from Birch-Murnaghan fourth-order equation of states (EOS) and the corresponding lattice parameter for each concentration are summarized in Table 1. It is clear that the equilibrium lattice constant is enlarged as the zinc concentration increases, due to the relatively larger radius of Zn^{2+} ion. Also, the symmetries are reduced by zinc doping. As the optical selection rule is closely related to the symmetry, zinc doping is expected to have profound influence on the optical excited state properties as we will discuss later.

Table 1 Equilibrium lattice constants (a_0), maximum displacements of O^{2-} (d_O) and Mg^{2+} (d_{Mg}) ions relative to pristine MgO, and point groups (PG) of $Mg_{1-x}Zn_xO$ at different zinc concentration

x	0	0.125	0.25	0.375	0.5
a_0 (Å)	4.23	4.25	4.27	4.28	4.30
d_O (Å)	–	0.05	0.09	0.16	0.19
d_{Mg} (Å)	–	0.04	0.07	0.10	0.13
PG	$O_h m3m$	$O_h m3m$	$D_{2h} mmm$	$C_{2h} 2/m$	D_{3d}

Lattice constants and displacements are in Angstrom

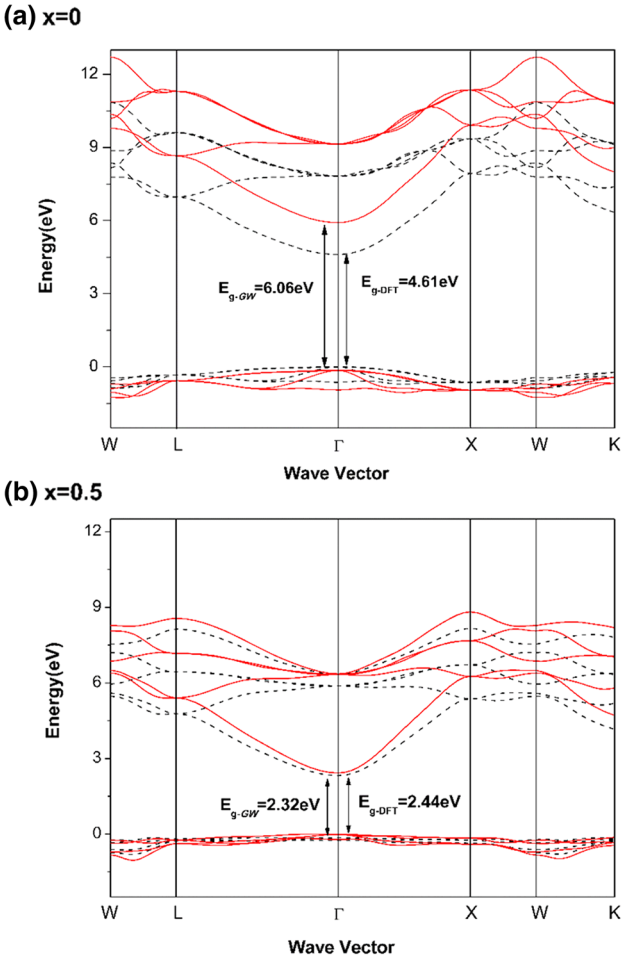

Fig. 2 Band structure of $Mg_{1-x}Zn_xO$ for $x = 0$ (MgO) and $x = 0.5$. *Black dashed lines* and *red solid lines* indicate results obtained from DFT and *GW* calculations, respectively. For clarity, only four valence and five conduction bands near the Fermi level are shown. The valence band maximum (VBM) has been shifted to 0 eV

Table 2 Band gaps from DFT and *GW* calculations of $Mg_{1-x}Zn_xO$ at different zinc concentration

x	0	0.125	0.25	0.375	0.5
E_g^{DFT} (eV)	4.61	3.70	3.19	2.79	2.32
E_g^{GW} (eV)	6.06	4.20	3.47	2.86	2.44

Band gaps are in eV

The band structures of $Mg_{1-x}Zn_xO$ of different doping concentrations are depicted in Fig. 2 and Supplementary Fig. S1, and the band gaps are summarized in Table 2. Our DFT calculation predicts a direct band gap of 4.61 eV at the Γ point of the first Brillouin zone, in good agreement with other work [29] but much lower than the experimental result of 7.8 eV [1] due to the inadequate treatment of electron–electron interac-

tion within the framework of DFT. More accurate results from the many-particle perturbation theory based on *GW* method show a direct band gap of 6.06 eV, much closer to the experimental value. This discrepancy is reasonable since we use the single-shot G_0W_0 method, the plasmon-pole approximation and a limited number of unoccupied bands in our calculation, to avoid the large computational cost of the *GW* method. The introduction of self-consistency, explicit treatment of the frequency-dependent dielectric function and the inclusion of more unoccupied bands will further improve the result [5], but this is not the topic of this work. From Table 2, it is clear that zinc doping significantly lowers the band gap of MgO, and the decrease in band gap is closely related to the concentration of zinc. In addition to the band gap reduction, the positions of valance band maxima (VBM) are also changed, while conduction band minima are fixed at the Γ point. For $Mg_{1-x}Zn_xO$ ($x = 0$, 0.25, and 0.375) the band gaps are direct at the Γ point, while for $Mg_{1-x}Zn_xO$ ($x = 0.125$ and 0.5), the band gaps are indirect as the VBM slightly shifted from the Γ point. On the other hand, the band dispersion is similar for all the different doping concentrations. The changes in band structure are also reflected in the total density of states (DOS) as depicted in Fig. 3, where the peak corresponding to the CBM shifts to lower energies as the concentration of the zinc doping increases. From Fig. 3, it is also noticeable that a new peak emerges at about 5 eV, and its intensity increases as zinc concentration increases; this is mainly the result of Zn 3*d* states as revealed by the partial density of states (PDOS) shown in Fig. 4 and Supplementary Fig. S2.

To investigate the influence of zinc doping on the electronic structure of $Mg_{1-x}Zn_xO$, we plot their PDOS values in Fig. 4 and Supplementary Fig. S2. The valence bands of pure MgO near the VBM are mainly composed of O 2*p* states, while the conduction bands near the CBM are composed of hybridized O 2*s* and Mg 3*s* states. Besides this new 3*d* peak at 5 eV, zinc doping does not have too much influence on the valence bands of $Mg_{1-x}Zn_xO$. However, the conduction bands near the CBM are significantly affected, showing strong hybridization among O 2*s*, Mg 3*s*, and Zn 4*s* states. The PDOS on the Mg 3*s* state decreasea to half of its original value when x increases from 0 to 0.5, while that of Zn 4*s* states is doubled. The reduction in band gap can be attributed to the hybridization between Zn 4*s* and O 2*s* states. Contrary to Mg, the chemical bonding between Zn and O is somewhat covalent. The hybridization between Zn and O atomic states forms bonding and antibonding states, and the bonding states shift the conduction band minimum (CBM) toward lower energies, reducing the band gap. As the contribution of the 4*s* state is on the edge of the conduction bands, the optical transitions may be significantly affected by zinc doping, as we will demonstrate in the following.

3.2 Optical properties

On the basis of the band structure corrected by the *GW* method, we explore the optical properties of $Mg_{1-x}Zn_xO$. We solve the Bethe–Salpeter equation in order to take into account the electron–hole interaction, so that a more accurate description of the optical properties will be obtained.

The imaginary part of the frequency-dependent dielectric function of the different materials are calculated, as this determines the optical absorption. In Fig. 5, this is shown for pure MgO ($x = 0$), and is compared with published experimental results [3,30]. Note that in Fig. 5, an energy shift of 1.72 eV (scissor operator) has been applied in order to compensate for the band gap underestimation. For a detailed discussion on the applicability and validity of the scissors operation, see Ref. [31], Chap. 15.3.3 and Chap. 20.2.1. From Fig. 5, it is clear that the electron–hole interaction has a significant impact on the dielectric function. Compared to the dielectric function obtained from the *GW*+RPA calculation, this does not include the electron–hole interaction, The results from the *GW*+BSE calculation show a clear red-shift, and agree much better with the experimental results, than with the values obtained from *GW*+RPA calculation.

In Fig. 6, we show the effect of zinc doping on the dielectric function $\varepsilon(\omega)$for $Mg_{1-x}Zn_xO$, with $x = 0$, 0.125, 0.25, 0.375, and 0.5. When the concentration of zinc increases, the peaks in the dielectric values shift toward lower energies, consistent with the aforementioned trend for the band gap. The first absorption peaks are located at 5.75, 4.67, 4.30, 3.65, and 3.23 eV for $x = 0$, 0.125, 0.25, 0.375, and 0.5, respectively. A more detailed analysis of peaks reveals that they result from bright excited states.

As indicated in Fig. 6, the optical transition of these states are between the different top valence bands and the lowest conduction band. For pure MgO ($x = 0$), the optical transition is located at the Γ point in the first Brillouin zone, while for the zinc-doped $Mg_{1-x}Zn_xO$, the optical transitions are no longer at the Γ point, due to the transition selections rules that are closely related to lattice symmetry. Also, for pure MgO, the first bright exciton is a bound exciton, i.e., the excitation energy is lower than the *GW* band gap, while for zinc-doped $Mg_{1-x}Zn_xO$, the excitons are resonant excitons excitation energies of which are higher than the corresponding *GW* band gaps, demonstrating the impact of zinc doping.

Table 3 shows the BSE-calculated results of the exciton energy, the exciton binding energy, and the exciton radius.

In Fig. 7, we plot the calculated bandgap values $E_{BG} = E_{xc} + E_b$ as a function of x. It is clear that the dependence is nonlinear; it can be described by the formula $E_{BG} = 6.0 - 13.7x + 13.7x^2$, where the factor 13.7 is the bowing factor. For rock-salt MgZnO, Schmidt-Grund et al. [27] experimentally found the following relationship: $E_{BG}(\text{eV}) = 7.6 - 7x + 7x^2$.

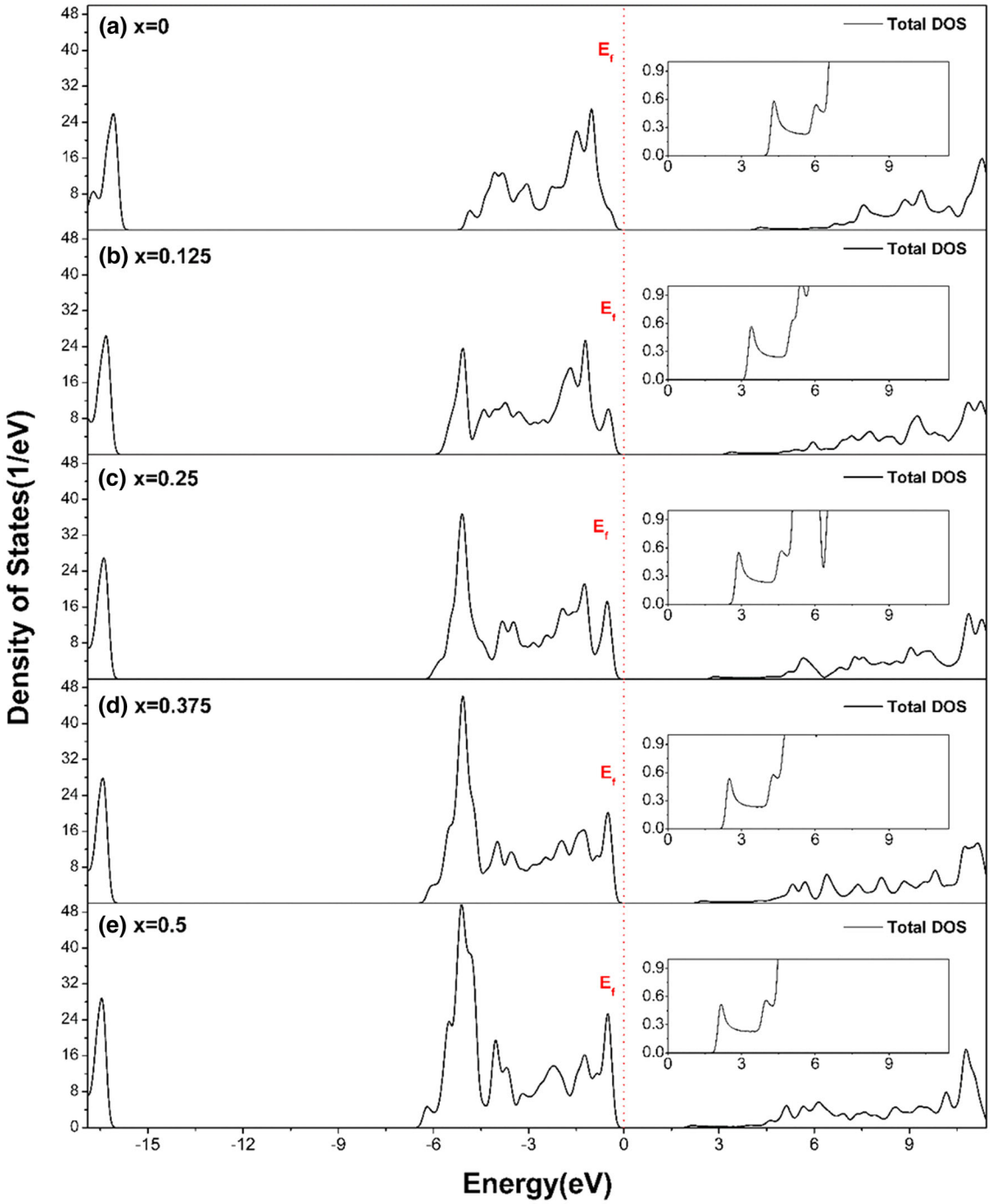

Fig. 3 Total density of states of $Mg_{1-x}Zn_xO$ (x = 0, 0.125, 0.25, 0.375 and 0.5). *Red dashed lines* indicate the Fermi levels. Like in Fig. 2, the VBM has been shifted to 0 eV. *Insets* density of states in the energy range of 0–9 eV plotted using a different y-axis scale

3.3 Exciton binding energies calculated using the hydrogen-like exciton model

As the exciton radii are much larger than the lattice constants, we have in all of these materials, a pure Wannier–Mott exciton, with an electron and a hole orbiting around a common center, while moving through the lattice. This can be described by a simple hydrogen- atom like model, and enables us to calculate the binding energy of the lowest exciton of $Mg_{1-x}Zn_xO$. In this case, the binding energy is given by [33]

$$E_b = E_n - E_g = \frac{\left(q^2/4\pi\varepsilon\varepsilon_0\right)}{2\left(\hbar^2/\mu\right)n^2} \tag{4}$$

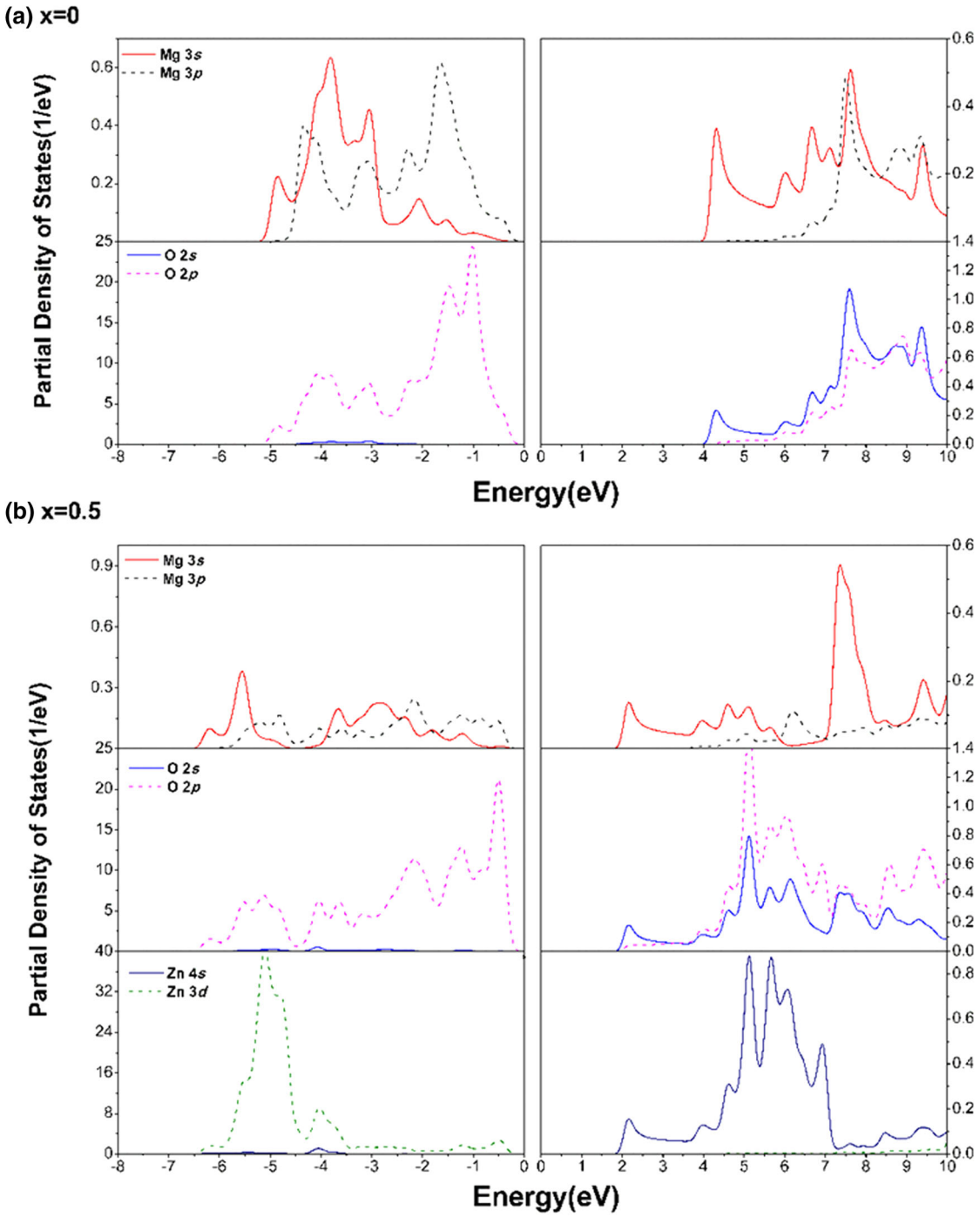

Fig. 4 Partial density of states for $Mg_{1-x}Zn_xO$ ($x = 0$ and 0.5). Note that different y-axis scales are used in the subplots

Here ε is the static dielectric constant, and μ is the reduced effective mass defined as

$$\mu = \frac{m_e^* m_h^*}{m_e^* + m_h^*} \tag{5}$$

where m_e^* and m_h^* are the effective masses of the electron and the hole, which are determined via

$$\frac{1}{m^*} = \frac{1}{\hbar^2}\frac{\partial^2 E(k)}{\partial k^2} \tag{6}$$

We can calculate the effective masses directly from the curvatures of the $E(k)$ diagrams, as shown in Fig. 2. We fit the energy dispersion graphs in the vicinity of the CBM and VBM with a fourth-order polynomial. For $x = 0$, the effective mass of the hole is about 10 times larger than that of the

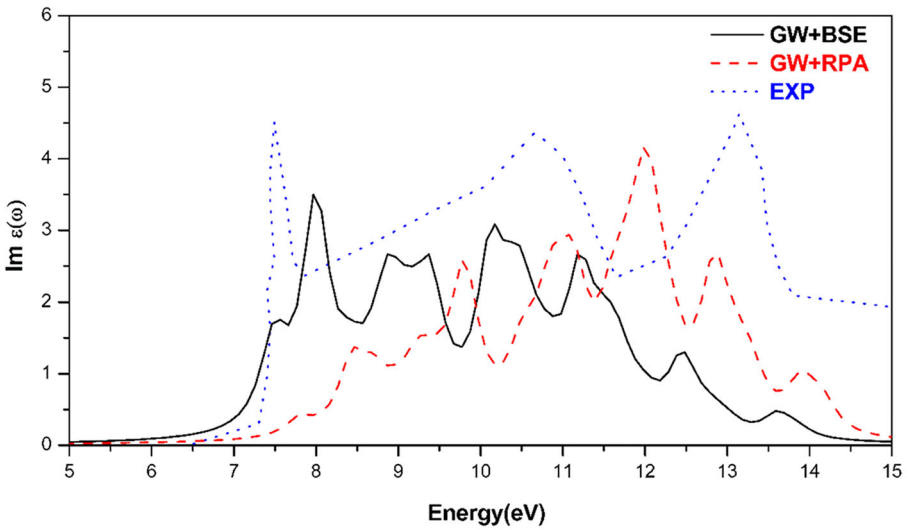

Fig. 5 Imaginary part of dielectric function for pure MgO. *Black solid*, *red dashed* and *blue dotted lines* indicate results from BSE and random phase approximation (RPA) calculations on top of *GW* band structure, and experimental results, respectively. Note that an energy shift of 1.72 eV has been applied in both *GW*+BSE and *GW*+RPA calculations in order to compensate the underestimation of band gap of the *GW* method. A Gaussian broadening of 0.2 eV has been applied [32]

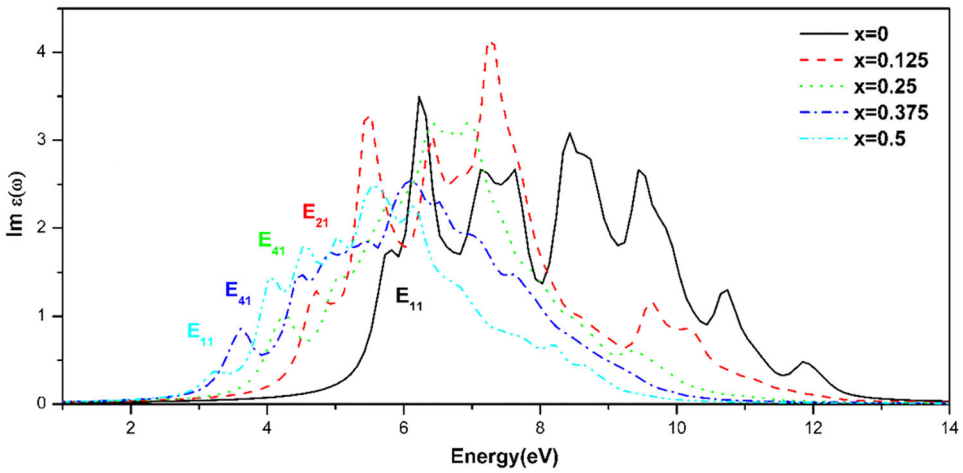

Fig. 6 Comparison of the imaginary part of $Mg_{1-x}Zn_xO$ (x = 0, 0.125, 0.25, 0.375, and 0.5). The labels E_{ij} denote the transitions corresponding to the first absorption peak. A Gaussian broadening of 0.2 eV has been applied

Table 3 Exciton energy (E_{xc}), binding energy (E_b) and radius (R) of the first exciton for $Mg_{1-x}Zn_xO$ (x = 0, 0.125, 0.25, 0.375 and 0.5)

x	0	0.125	0.25	0.375	0.5
E_{xc} (eV)	5.75	3.92	3.21	2.64	2.23
E_b (meV)	310	280	260	220	210
R (nm)	2.97	3.02	3.05	3.12	3.13

electron, while for increasing x values, the mass becomes even larger. Therefore, although the valence band curvature is difficult to match for $x > 0$, this does not have a strong effect on the accuracy of the effective exciton mass, as this is then dominated by that of the electron.

We have calculated the static dielectric constants via RPA using DFT wave functions and energies [25]. The real parts of the dielectric function for $Mg_{1-x}Zn_xO$ (x=0, 0.125, 0.25, 0.375, and 0.5) are shown in the supplementary information

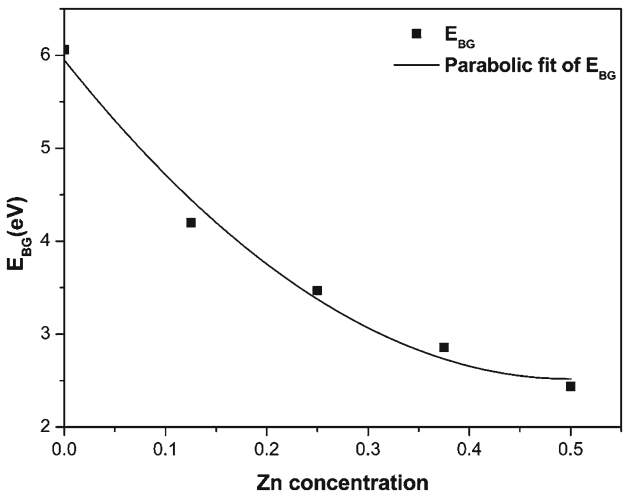

Fig. 7 Parabolic fit of the bandgap energy $E_{BG} = E_{xc} + E_b$ as a function of doping concentration

Table 4 Calculated reduced effective masses (μ), calculated static dielectric constants (ε) and binding energy of the first exciton, for $Mg_{1-x}Zn_xO$ ($x = 0, 0.125, 0.25, 0.375$ and 0.5) using the hydrogen-like atom model; the effective mass is relative to that of an electron

x	0	0.125	0.25	0.375	0.5
μ	0.319	0.313	0.301	0.282	0.269
ε	3.920	4.188	4.470	4.775	5.100
E_b (meV)	282	243	205	168	141

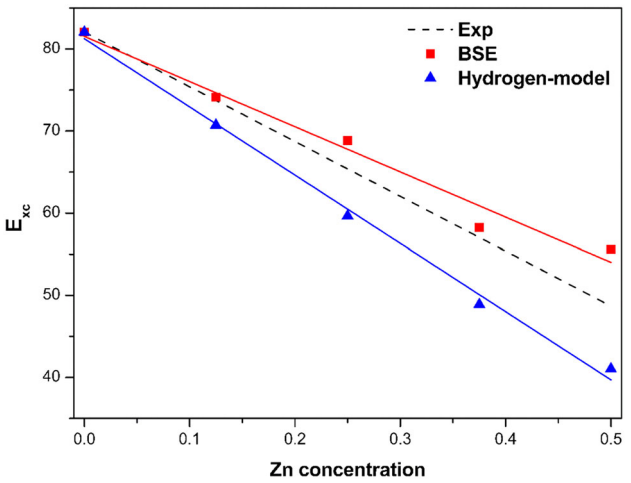

Fig. 8 Plot of the binding energy obtained by BSE and the hydrogen-like atom model, respectively, for the first exciton as a function of zinc concentration of rock-salt MgZnO; the data points are scaled to correspond to 85 meV at $x = 0$. The *red filled squares* and the *blue filled triangles* indicate the data points for the binding energies obtained from the BSE and the hydrogen-like atom model, respectively. The *dotted line* shows the published experimental results for rock-salt MgZnO [27]

in Supplementary Fig. S3. Following Schleife [32], initially we use the real part of the dielectric function at $\omega = 0$ as the effective dielectric constant for the exciton. The resulting exciton binding energy values are then given in Table 4, together with the calculated values for $\varepsilon(\omega = 0)$ and μ. For pristine MgO ($x = 0$), the hydrogen-like atom model predicts a binding energy of 282 meV, which is only 28 meV smaller than the binding energy predicted by the BSE calculation. The binding energies decrease again almost linearly as the doping concentration of zinc increases, just as in the case of the BSE calculation. However, the difference with the BSE results becomes larger for larger zinc concentration, possibly due to the singularities in the band structure at VBM, violating the parabolic energy dispersion relation [31].

Figure 8 shows the binding energies versus zinc concentration x, both calculated by the BSE method (scaled), and the hydrogen-like atom model (scaled) and are compared with the experimental results [27] obtained with rock-salt MgZnO (scaled).

3.4 Discussion

From the results of the BSE model, it is clear that the use of the Bethe–Salpeter Equation (BSE) is an essential step to obtain the absorption spectra; they clearly show the generation of excitons near the bandgap. We also conclude from the literature [31] that the BSE values calculated for the exciton binding energy are strongly overestimated (factor of 4). The values are similar to those calculated, when using the simple exciton hydrogen model, after calculating the effective masses from the energy band curvature.

The weak point in both approaches is the value of the screening constant $\varepsilon(\omega = 0)$ that is used. As pointed out by Bechstedt in his chapter on dynamic effects [31], in fact for MgO and ZnO, an effective higher value ε_{eff} has to be used, because the exciton binding energy is no longer much smaller than the phonon energies. As the exciton binding energy scales with the square of the screening factor, this means that the effective value for MgO is much larger than the calculated static value.

Unfortunately, not many experimental results are available for the $Mg_{1-x}Zn_xO$ materials. Using ellipsometry of rock-salt $Mg_xZn_{1-x}O(0.68 \leq x \leq 1)$, Schmidt-Grund et al. [27] found that the change of the exciton binding energy with x is indeed linear for rock-salt type MgZnO. The dependence found by Schmidt-Grund et al. is inserted in Fig. 8. From the comparison, we conclude that the results obtained using the *GW*+BSE model fit the data of Schmidt-Grund very well, while those calculated from the band curvature and the hydrogen model underestimate the exciton binding energies.

Additional experimental results are needed, especially using synchrotron excitation and fluorescence emission detection, as a function of temperature, similar to those obtained for doped MgO [34].

4 Conclusions

In summary, we have investigated the electronic structural and optical properties of zinc-doped MgO utilizing the *GW* method combined with Bethe–Salpeter equation to include the electron–hole interaction. We find that zinc doping introduces deep valence states from Zn 3*d* states; the conduction bands near the Fermi level due to Zn 4*s* states will significantly lower the band gap, the position of the first absorption peak, the energy of the first exciton, and the exciton binding energy. Zinc doping also reduces the lattice symmetry, which affects the optical properties through transition selection rules.

We have shown how the exciton energy can be tuned by doping with zinc, for rock-salt type of $Mg_{1-x}Zn_xO$ with $x < 0.5$. This will enable the future development of tunable deep UV emitters. We have also shown that the exciton

binding energy in these materials is high enough to make them stable at room temperature, and that the hydrogen-like exciton model can be used to calculate the exciton binding energies.

For the future use of $Mg_{1-x}Zn_xO$ as deep UV-light sources, further analysis is required. A detailed investigation of allowed transitions is needed, including the competing process of Auger electron emission from triplet states.

We conclude that the BSE method of calculating the exciton binding energies, are quite accurate. The results obtained by means of the hydrogen-like exciton model appear to be adequate to calculate the trend in the change of the exciton binding energy, when doping an oxide like MgO with ZnO, while reducing strongly the amount of computer power needed. Therefore, the hydrogen-like exciton model, including the calculation of the *GW*+RPA band diagrams, can be considered as an important tool to optimize the doping of mixed oxides for UV devices and predict its change in optical characteristics by doping. However, the complete solution of the Bethe– Salpeter Equation (BSE), plus scaling of the screening factor, is needed to closely match the known experimental data of the exciton binding energy in rock-salt MgZnO.

Acknowledgments This research is supported by the National Natural Science Foundation of China (61271053) and Innovation in Higher Education Disciplines Introduction Program (B07027). The authors appreciate the computational resources provided by Shanghai Supercomputer Center.

References

1. Whited, R.C., Flaten, C.J., Walker, W.C.: Exciton thermoreflectance of MgO and CaO. Solid State Commun. **13**, 1903–1905 (1973)
2. Yoshikawa, H., Adachi, S.: Optical constants of ZnO. Jpn. J. Appl. Phys. **36**, 6237–6243 (1997)
3. Roessler, D.M., Walker, W.C.: Electronic spectrum and ultraviolet optical properties of cCrystalline MgO. Phys. Rev. **159**, 733–738 (1967)
4. Hümmer, K.: Interband magnetoreflection of ZnO. Phys. Status Solidi B **56**, 249–260 (1973)
5. Han, S., Zhang, J., Zhang, Z., Zhao, Y., Wang, L., Zheng, J., Yao, B., Zhao, D., Shen, D.: $Mg_{0.58}Zn_{0.42}O$ thin films on MgO substrates with MgO buffer layer. ACS Appl. Mater. Interfaces **2**, 1918–1921 (2010)
6. Lim, J.-H., Kang, C.-K., Kim, K.-K., Park, I.-K., Hwang, D.-K., Park, S.-J.: UV electroluminescence emission from ZnO light-emitting diodes grown by high-temperature radiofrequency sputtering. Adv. Mater. **18**, 2720–2724 (2006)
7. Tennakone, K., Bandara, J., Bandaranayake, P.K.M., Kumara, G.R.A., Konno, A.: Enhanced efficiency of a dye-sensitized solar cell made from MgO-coated nanocrystalline SnO_2. Jpn. J. Appl. Phys. **40**, L732–L734 (2001)
8. Hsu, H.-C., Wu, C.-Y., Cheng, H.-M., Hsieh, W.-F.: Band gap engineering and stimulated emission of ZnMgO nanowires. Appl. Phys. Lett. **89**, 013101 (2006)
9. Yoo, J., Chon, B., Tang, W., Joo, T., Dang, L.S., Yi, G.-C.: Excitonic origin of enhanced luminescence quantum efficiency in MgZnO/ZnO coaxial nanowire heterostructures. Appl. Phys. Lett. **100**, 223103 (2012)
10. Hu, Y., Cai, B., Hu, Z., Liu, Y., Zhang, S., Zeng, H.: The impact of Mg content on the structural, electrical and optical properties of MgZnO alloys: a first principles study. Curr. Appl. Phys. **15**, 423–428 (2015)
11. Amrani, B., Ahmed, R., El, : Haj Hassan, F.: Structural, electronic and thermodynamic properties of wide band gap $Mg_xZn_{1-x}O$ alloy. Comput. Mater. Sci. **40**, 66–72 (2007)
12. Hohenberg, P., Kohn, W.: Inhomogeneous electron gas. Phys. Rev. **136**, B864–B871 (1964)
13. Kohn, W., Sham, L.J.: Self-consistent equations including exchange and correlation effects. Phys. Rev. **140**, A1133–A1138 (1965)
14. Hybertsen, M.S., Louie, S.G.: Electron correlation in semiconductors and insulators: band gaps and quasiparticle energies. Phys. Rev. B. **34**, 5390–5413 (1986)
15. Rohlfing, M., Louie, S.G.: Electron–hole excitations and optical spectra from first principles. Phys. Rev. B. **62**, 4927–4944 (2000)
16. Monkhorst, H.J., Pack, J.D.: Special points for Brillouin-zone integrations. Phys. Rev. B. **13**, 5188–5192 (1976)
17. Troullier, N., Martins, J.L.: Efficient pseudopotentials for plane-wave calculations. Phys. Rev. B. **43**, 1993–2006 (1991)
18. Perdew, J.P., Burke, K., Ernzerhof, M.: Generalized gradient approximation made simple. Phys. Rev. Lett. **77**, 3865–3868 (1996)
19. Hedin, L.: New method for calculating the one-particle Green's function with application to the electron-gas problem. Phys. Rev. **139**, A796–A823 (1965)
20. Hedin, L.: On correlation effects in electron spectroscopies and the *GW* approximation. J. Phys. Condens. Matter **11**, R489 (1999)
21. Godby, R.W., Needs, R.J.: Metal–insulator transition in Kohn–Sham theory and quasiparticle theory. Phys. Rev. Lett. **62**, 1169–1172 (1989)
22. Oschlies, A., Godby, R.W., Needs, R.J.: GW self-energy calculations of carrier-induced band-gap narrowing in *n*-type silicon. Phys. Rev. B **51**, 1527–1535 (1995)
23. Salpeter, E.E., Bethe, H.A.: A relativistic equation for bound-state problems. Phys. Rev. **84**, 1232–1242 (1951)
24. Strinati, G.: Effects of dynamical screening on resonances at inner-shell thresholds in semiconductors. Phys. Rev. B **29**, 5718–5726 (1984)
25. Marini, A., Hogan, C., Grüning, M., Varsano, D.: Yambo: an ab initio tool for excited state calculations. Comput. Phys. Commun. **180**, 1392–1403 (2009)
26. Giannozzi, P., Baroni, S., Bonini, N., Calandra, M., Car, R., Cavazzoni, C., Ceresoli, D., Chiarotti, G.L., Cococcioni, M., Dabo, I., Corso, A.D., de Gironcoli, S., Fabris, S., Fratesi, G., Gebauer, R., Gerstmann, U., Gougoussis, C., Kokalj, A., Lazzeri, M., Martin-Samos, L., Marzari, N., Mauri, F., Mazzarello, R., Paolini, S., Pasquarello, A., Paulatto, L., Sbraccia, C., Scandolo, S., Sclauzero, G., Seitsonen, A.P., Smogunov, A., Umari, P., Wentzcovitch, R.M.: QUANTUM ESPRESSO: a modular and open-source software project for quantum simulations of materials. J. Phys. Condens. Matter **21**, 395502 (2009)
27. Schmidt-Grund, R., Carstens, A., Rheinländer, B., Spemann, D., Hochmut, H., Zimmermann, G., Lorenz, M., Grundmann, M., Herzinger, C.M., Schubert, M.: Refractive indices and band-gap

properties of rocksalt $Mg_xZn_{1-x}O$ ($0.68 \leq x \leq 1$). J. Appl. Phys. **99**, 123701 (2006)
28. Maznichenko, I.V., Ernst, A., Bouhassoune, M., Henk, J., Däne, M., Lüders, M., Bruno, P., Hergert, W., Mertig, I., Szotek, Z., Temmerman, W.M.: Structural phase transitions and fundamental band gaps of $Mg_xZn_{1-x}O$ alloys from first principles. Phys. Rev. B **80**, 144101 (2009)
29. Fritsch, D., Schmidt, H., Grundmann, M.: Pseudopotential band structures of rocksalt MgO, ZnO, and $Mg_{1-x}Zn_xO$. Appl. Phys. Lett. **88**, 134104 (2006)
30. Li, Q., Tu, Y., Yang, L., Tolner, H.: Deep-UV exciton emission from $Mg_{1-x}rmCa_xO$—a first-principle investigation. J. Soc. Inf. Disp. **22**, 564–571 (2014)
31. Bechstedt, F.: Many-Body Approach to Electronic Excitations. Springer, Berlin and Heidelberg (2015)
32. Schleife, A., Roedl, C., Fuchs, F., Furthmueller, J., Bechstedt, F.: Optical and energy-loss spectra of MgO, ZnO, and CdO from ab initio many-body calculations. Phys. Rev. B **80**, 035112 (2009)
33. Huang, K., Han, R.: Solid State Physics. Higher Education Press, Beijing (1988)
34. Kuang, W.-J., Li, Q., Chen, Y.-X., Hu, K., Wang, N.-H., Xing, F.-L., Yan, Q., Sun, S.-S., Huang, Yan, Tao, Y., Tolner, H.: Surface exciton emission of MgO crystals. J. Phys Appl. Phys. **46**, 365501 (2013)